INT. J. NUM. METH. HEAT FLUID FLOW, VOL. 2, 335–358 (1992)

HEAT AND FLUID FLOW AT ENTRANCE REGIONS OF ROTATING ISO-HEAT FLUX CHANNELS WITH LAMINAR THROUGHFLOW

SHIN FANN AND WEN-JEI YANG

Department of Mechanical Engineering and Applied Mechanics, University of Michigan, Ann Arbor, Michigan 48109, USA

AND

S. MOCHIZUKI

Department of Mechanical Systems Engineering, Tokyo University of Agriculture and Technology, Koganei, Tokyo, Japan

ABSTRACT

A theoretical study is performed on three-dimensional, heat transfer and fluid flow in radially rotating heated channels with steady, laminar throughflow. Consideration is given to the channel of different geometry. Both the rotational speed and throughflow rate are varied. The flow is hydrodynamically and thermally developing, with a constant wall heat flux. The velocity–vorticity method is employed in the formulation and numerical results are obtained by means of a finite-difference technique. The Nusselt number, friction factor, and temperature and velocity distributions are determined, and the role of the Coriolis force on the entrance-region transport phenomena is investigated. Results are compared with the existing literature.

KEY WORDS Velocity–vorticity method Iso-heat flux channels Laminar flow Rotating systems

NOMENCLATURE

a	channel height in the y-direction (m)
b	channel width in the z-direction (m)
C_p	specific heat (kJ/kg °C)
f	friction factor
Gr	rotational Grashof number for iso-flux case $= \dfrac{\Omega^2 L_x \beta q_w a^4}{k\nu^2}$
H	distance from rotational axis to inlet or distance (m)
h	convective heat transfer coefficient (W/m² °C)
h^*	non-dimensional distance from rotational axis to inlet or distance from rotational axis to fully-developed region, $= H/a$
k	thermal conductivity of fluid (W/m °C)
L_x	characteristic length in the x-direction (in terms of duct height) (m)
Nu_x	locally-averaged Nusselt number over a wall, $= ha/k$
Nu	circumferentially-averaged Nusselt number

0961–5539/92/040335–24$2.00

Received July 1991
Revised March 1992

P	pressure (Pa)
P^*	reduced pressure (Pa)
p	dimensionless reduced pressure
Pr	Prandtl number, $= \nu/\alpha$
q_w	local wall heat flux (W/m^2)
Re	Reynolds number, $= U_0 a/\nu$
Ro	Rossby number, $\Omega a/U_0$
Ta	Taylor number, $= \Omega a^2/\nu = ReRo$
T_0	inlet mean temperature (°C)
T	temperature (°C)
T_w	wall temperature (°C)
U, V, W	velocity components in the x-, y-, z-directions, respectively (m/sec)
U_0	inlet mean velocity (m/sec)
u, v, w	dimensionless velocity components
X	distance in the axial direction measured from flow inlet (m)
Y	coordinate in the direction of rotation (m)
Z	distance along rotational axis (m)
x, y, z	dimensionless coordinate system with origin at centre of channel cross-section
x', y', z'	dimensionless coordinate system with origin at intersection of left side wall and trailing wall

Greek

α	thermal diffusivity of fluid, $= k/\rho C_p$ (m^2/sec)
β	thermal expansion coefficient (K^{-1})
η	length ratio, $= L_x/a$
μ	dynamic viscosity (kg/m-sec)
ν	kinematic viscosity (m^2/sec)
ρ	fluid density (kg/m^3)
θ	dimensionless temperature, $= (T - T_0)/(T_w - T_0)$
Ω	angular velocity of rotation (sec^{-1})
Ξ	axial vorticity (sec^{-1})
ξ	non-dimensional axial vorticity
ζ	aspect ratio, $= b/a$

Subscripts

c	characteristic quantity
0	at inlet
w	on wall
x	local value at x

Superscripts

*	reduced or presumed value
—	vector or averaged value

INTRODUCTION

The influences of rotation on earth, such as geostrophic vortex and ocean flow, have stimulated scientists to investigate similar physical phenomena occurring in engineering applications, such as flows in a rotary pump, gas turbine and other rotating systems[1,2]. There are four types of rotation or revolution applied in engineering[3]: radial rotation, parallel revolution, axial rotation and circumferential revolution.

Barua[4] made one of the earliest attempts to theoretically simulate a fully-developed, laminar flow through a pipe in the radial rotation. Results obtained by an approximate series solution were valid for a small angular velocity. Trefethen[5] conducted an experimental investigation to determine the influence of radial rotation on flow resistance in circular tubes. The friction factor was obtained for both the laminar and turbulent regimes. Benton and Boyer[6], Mori and Nakayama[7] and Ito and Nanbu[8] theoretically analysed a developed, laminar flow, assuming that the flow consisted of a central core with a relatively thin boundary layer in the immediate vicinity of the wall. An experimental study on the effect of radial rotation on heat transfer was performed by Mori *et al.*[9]. Johnston *et al.*[10] conducted experiments on a fully-developed, turbulent flow in a channel rotating radially at a steady speed and found three stability-related phenomena: (i) a reduction (increase) in the rate of wall-layer stream bursting in locally stabilized (destabilized) wall layers; (ii) a total suppression of transition to turbulence in a stabilized layer; (iii) development of large-scale roll cells on the destabilized side of the channel due to the growth of a Taylor–Gortler vortex instability. They suggested that local effects of rotational stabilization could be related to the Richardson number.

Skiadaressis and Spalding[11] considered a heated flow in either the laminar or turbulent flow range and derived a numerical method based on the works of Patankar and Spalding[12] and Majumdar *et al.*[13]. Vidyanidhi *et al.*[14] substituted the theoretical velocity profiles, obtained by Barua[4] for an isothermal, developed flow, into the energy equation to determine the temperature profile for a uniformly heated wall case. An experimental study for heat transfer in the entrance region was performed by Metzger and Stan[15]. Results were obtained for laminar heat transfer with parallel-mode rotation. A transient method was used in which a disc with a series of radial holes was pre-heated prior to rotation and a coolant flowed through the radial holes during the test. Howard *et al.*[16] developed a parabolic numerical procedure, an extension of Patankar and Spalding[12] and Majumdar *et al.*[13], to study a flow in a straight, radially rotating channel of rectangular cross-sections, chosen as a simple model of an impeller passage. The $\kappa-\varepsilon$ turbulence model was employed, with three alternative modifications, to include the influence of the Coriolis force on turbulent kinetic energy. The Coriolis effect was assumed to be confined inside the boundary layers.

Morris[17] provided a detailed review of several important documents published before 1981 and conducted experiments to investigate the influence of rotation on heat transfer in tubes with either the radial- or parallel-mode rotation. It was disclosed that irrespective of the rate of flow through a radially rotating tube, an increase in the heat flux resulted in a retardation of both the local heat transfer and mean Nusselt number in the radial outflow case but an enhancement in the inward flow case. Morris and Ayhan[18] investigated the turbulent heat transfer for both the outward and inward flows in a radially rotating tube using several heat transfer correlation equations. Harasgama and Morris[19] studied the influence of rotation (especially the secondary flow and centripetal buoyancy) on the heat transfer characteristics of circular, triangular, and square coolant passages. It was revealed that an increase in the centripetal buoyancy tended to decrease the average heat transfer performance in the radial outward flow case, but the opposite was true in the inward flow case, where the leading (suction) side heat transfer was enhanced while the trailing (pressure) side heat transfer decreased.

Speziale[20] and Speziale and Thangam[21] solved time-dependent laminar flow in rotating rectangular ducts using a finite difference method to examine the secondary flow and roll-cell instability problem in rotating channel flows. A substantial distortion of axial velocity profiles

was found in the roll-cell and Taylor–Proundman regimes. Siegal[22] performed a numerical study to determine the buoyancy effect on a fully developed radially laminar outward or inward flow. Both the velocities and temperature were expanded in power series using the Taylor number as a perturbation parameter. Mansour[23] also conducted a numerical analysis on a fully-developed, steady, laminar flow through a slowly rotating pipe. The solution was expanded into a power series of low Reynolds number having a combined similarity parameter as the exponent. Iacovides and Launder[24] developed a finite-volume method to simulate a turbulent flow in a rotating square-sectioned duct. Two turbulent models were employed to represent turbulent stresses and heat fluxes in the mean part of the flow: the standard k–ε eddy-viscosity model (EVM) and an algebraic second-moment closure (ASM). In the semi-viscous sublayer adjacent to the wall, a generalization of Van Driest's version of the mixing-length hypothesis was adopted. Following the previous work, Iacovides and Launder[25] numerically studied the fully-developed flow and heat transfer for various aspect ratios and parameters.

Both the experimental and numerical results were obtained for flows in a rectangular duct rotating about an orthogonal axis[26]. The test section was heated by a radiative flux. The wall temperatures were measured using thermocouples and the infra-red pyrometer technique. The problem was also analysed theoretically using three-dimensional equations (with mixing length model of turbulence) which were numerically solved by the ADI method. Hwang and Jen[27] reported a theoretical investigation of heat transfer in a hydrodynamically and thermally fully-developed flow inside a rotating isothermal ducts. The temperature distribution equation for fully-developed flow in a non-rotating passage[28] was modified to estimate the temperature field in the rotating duct. Numerical results were obtained by Durst and Raszillier[29]. The perturbation of the Hagen–Poiseuille flow, produced by the pipe rotation, was computed to the secondary order. Raszillier *et al.*[30] got a perturbation solution for a fully developed flow through a rotating pipe. Two coupled non-linear equations for the axial velocity and the stream function f of the transverse flow led to an infinite system of linear equations.

Recently, heat transfer in a multipass serpentine type flow passage was experimentally studied[31]. It was found that the minimum level of heat transfer attained could be well predicted by Kays' laminar flat plate correlation[32] and that the centripetal buoyancy limited the laminarization process. Wagner *et al.*[33] performed experiments, using a smooth wall, large scale heat transfer model, to determine the effects of rotation on heat transfer inside internal coolant passages. Rotation was found to affect the heat transfer coefficients differently at different locations inside the coolant passages. In another experiment on heat transfer in rotating serpentine passages, the buoyancy and Coriolis forces, respectively, caused the local heat transfer coefficients to decrease by as much as 60% and to increase by 250% from the corresponding values at no rotation. The effects of the rib turbulators and the aspect ratio on heat transfer in flows inside rectangular channels and multipass channels were investigated[35–38].

The present study treats the transport phenomena in a radially outward flow inside ducts with uniform wall heat flux. The flow is hydrodynamically and thermally developing. A formulation by the velocity–vorticity method[39,40] is employed to avoid dealing with the pressure terms. The transverse velocities are determined directly from two Poisson's equations, which are derived from the axial vorticity and the continuity equation. The equation in the form of parabolic flow[12,41] is employed to solve the axial velocity, axial vorticity and temperature explicitly.

THEORETICAL ANALYSIS

Consider a forced flow through a heated rectangular duct which rotates at a constant speed about an axis normal to the longitudinal direction of the duct. The physical configuration and the coordinate system are shown in *Figure 1*. The following assumptions are imposed in the formulation of the problem based on the characteristics of the flow[7,16,17,27,32]:

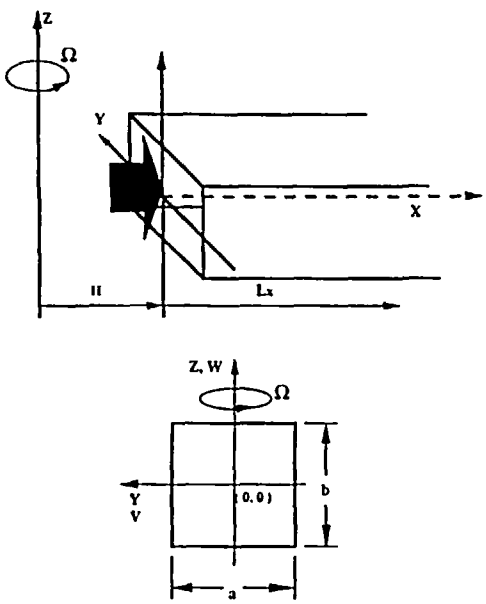

Figure 1 Coordinate system on rotating channel

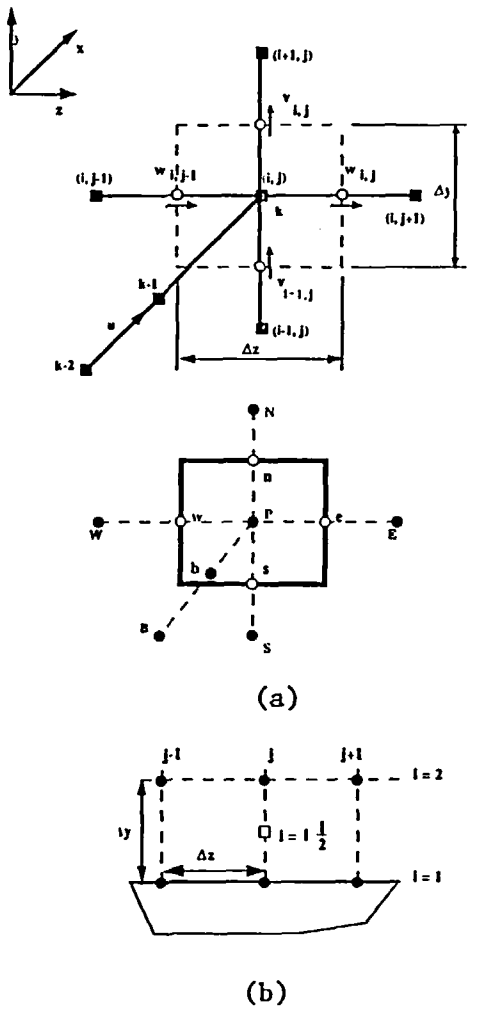

Figure 2 Grid systems, (a) staggered mesh and nodes and (b) meshes and nodes for boundary vorticity analysis

(a) incompressible, laminar, steady flow;
(b) relatively high Reynolds number ($Re \geqslant 100$);
(c) constant fluid properties (except fluid density);
(d) Boussinesq's approximation applicable;
(e) constant heat flux at walls (iso-flux case);
(f) uniform inlet velocity and uniform inlet fluid temperature (hydrodynamically and thermally developing flow field); and
(g) axial conduction negligible.

The components of the Coriolis acceleration terms in the X- and Y-directions are $-2WV$ and $2WU$, respectively. Notice that there is no Coriolis acceleration component in the Z-direction in the radially rotating case.

In the Boussinesq's approximation, the buoyancy force is important in the momentum equations. With the definition of thermal expansion coefficient as $\beta = -(1/\rho)(\partial\rho/\partial T)$, the local density can be approximated to be:

$$\rho = \rho_0[1 - \beta(T - T_0)]$$

where ρ_0 is fluid density at inlet temperature, T_0.

The following characteristic quantities are introduced for the order of magnitude analysis;

$$X_c = L_x, \quad Y_c = a, \quad Z_c = b, \quad U_c = U_0, \quad V_c = W_c = (U_0/\eta)$$
$$T_c = q_w a/k, \quad P_c = \mu(U_0/a)$$

where U_0 is the uniform inlet axial velocity. The characteristic temperature is defined based on the heat flux q_w. All physical quantities are reduced to the dimensionless form as:

$$x = \frac{X}{X_c}, \quad y = \frac{Y}{a}, \quad z = \frac{Z}{b}, \quad u = \frac{U}{U_0}, \quad v = \frac{V}{V_c}, \quad w = \frac{W}{W_c}, \quad p = \frac{P^*}{P_c}$$
$$\theta = \frac{T - T_0}{T_c}, \quad \eta = \frac{L_x}{a}, \quad \zeta = \frac{b}{a}$$

The Grashof number is defined based on heat flux.

The viscous heating is negligible in an incompressible flow. The length ratio, η, in the entrance region is not large enough to neglect the convective terms in the momentum and energy equations. For the Reynolds number exceeding 100 and the Prandtl number greater than 0.1, the axial conduction in the energy equation can be neglected. The dissipation terms can be neglected in an incompressible flow. The simplified governing equations read:

Continuity equation

$$\frac{\partial u}{\partial x} + \frac{\partial v}{\partial y} + \frac{1}{\zeta}\frac{\partial w}{\partial z} = 0 \tag{1}$$

Momentum equations

x-direction:

$$u\frac{\partial u}{\partial x} + v\frac{\partial u}{\partial y} + \left(\frac{1}{\zeta}\right)w\frac{\partial u}{\partial z} = \frac{-1}{Re}\frac{\partial p}{\partial x} + 2Rov - \left(\frac{\eta Gr}{Re^2}\right)\theta\left(x + \frac{h^*}{\eta}\right) + \left(\frac{\eta}{Re}\right)\frac{\partial^2 u}{\partial y^2} + \left(\frac{\eta}{\zeta^2 Re}\right)\frac{\partial^2 u}{\partial z^2} \tag{2}$$

y-direction:

$$u\frac{\partial v}{\partial x} + v\frac{\partial v}{\partial y} + \left(\frac{1}{\zeta}\right)w\frac{\partial v}{\partial z} = \frac{-\eta^2}{Re}\frac{\partial p}{\partial y} - 2\eta^2 Rou - \left(\frac{\eta Gr}{Re^2}\right)\theta y + \left(\frac{\eta}{Re}\right)\frac{\partial^2 v}{\partial y^2} + \left(\frac{\eta}{\zeta^2 Re}\right)\frac{\partial^2 y}{\partial z^2} \tag{3}$$

z-direction:

$$u\frac{\partial w}{\partial x} + v\frac{\partial w}{\partial y} + \left(\frac{1}{\zeta}\right)w\frac{\partial w}{\partial z} = \frac{-\eta^2}{\zeta Re}\frac{\partial p}{\partial z} + \left(\frac{\eta}{Re}\right)\frac{\partial^2 w}{\partial y^2} + \left(\frac{\eta}{\zeta^2 Re}\right)\frac{\partial^2 w}{\partial z^2} \tag{4}$$

Energy equation

$$u\frac{\partial \theta}{\partial x} + v\frac{\partial \theta}{\partial y} + \left(\frac{1}{\zeta}\right)2\frac{\partial \theta}{\partial z} = \left(\frac{\eta}{PrRe}\right)\frac{\partial^2 \theta}{\partial y^2} + \left(\frac{\eta}{\zeta^2 PrRe}\right)\frac{\partial^2 \theta}{\partial z^2} \tag{5}$$

The vorticity and characteristic vorticity in the axial direction are defined as:

$$\Xi = \frac{\partial W}{\partial Y} - \frac{\partial V}{\partial Z}$$

and

$$\xi_c = \frac{U_0}{\eta a}$$

respectively. The non-dimensional axial vorticity can be written as:

$$\xi = \frac{\partial w}{\partial y} - \frac{1}{\zeta}\frac{\partial v}{\partial z} \tag{6}$$

In order to derive the axial vorticity transport equation, (3) is differentiated with respect to z, followed by multiplying by $(1/\zeta)$. Equation (4) is then differentiated with respect to y. Subtracting the two resulting equations to eliminate the pressure terms, one obtains the axial vorticity transport equation as:

$$u\frac{\partial \xi}{\partial x} + v\frac{\partial \xi}{\partial y} + \left(\frac{1}{\zeta}\right)w\frac{\partial \xi}{\partial z} = 2\eta^2 Ro\frac{\partial u}{\partial z} + \left(\frac{\eta Gr}{Re^2}\right)y\frac{\partial \theta}{\partial z} + \left(\frac{\eta}{Re}\right)\frac{\partial^2 \xi}{\partial y^2} + \left(\frac{\eta}{\zeta^2 Re}\right)\frac{\partial^2 \xi}{\partial z^2} \tag{7}$$

Since the flow is three-dimensional, it is not appropriate to employ the steam function here. In order to determine the transverse velocities, two equations in the elliptic form are derived from the continuity equation and the definition of axial vorticity. To derive the equation for v, (1) is differentiated with respect to z and then combined with the continuity equation to eliminate the w terms. The equation for w can be derived in a similar manner. The resulting transverse velocity equations are:

$$\frac{\partial^2 v}{\partial y^2} + \frac{1}{\zeta^2}\frac{\partial^2 v}{\partial z^2} = -\frac{1}{\zeta}\frac{\partial \xi}{\partial z} - \frac{\partial^2 u}{\partial x\,\partial y} \tag{8}$$

$$\frac{\partial^2 w}{\partial y^2} + \frac{1}{\zeta^2}\frac{\partial^2 w}{\partial z^2} = \frac{\partial \xi}{\partial y} - \frac{1}{\zeta}\frac{\partial^2 u}{\partial x\,\partial z} \tag{9}$$

In summary, the governing equations for fluid flow include: (i) the continuity equation (1), (ii) the axial velocity equation (2), (iii) the axial vorticity equation (7), and (iv) the transverse velocity equations (8) and (9). They are of parabolic–elliptic form. This formulation is called the velocity–vorticity method. Flow temperature is solved by the energy equation, (5). The following boundary conditions are used:

$$\begin{aligned} &u = 1.0, \quad v = w = 0, \quad \theta = 0, \quad \xi = 0 \quad \text{at inlet} \\ &u = v = w = 0, \quad \partial\theta/\partial n = -1.0 \quad \text{at walls} \end{aligned} \tag{10}$$

where n represents the normal direction of walls. No boundary condition is specified at downstream section. In the initial stage of study, it is uncertain whether or not the fluid flow is symmetric with respect to the centreline ($z' = 0.5$) of the channel cross-section within the distance studied. After many numerical experiments, the symmetry in the fluid flow was disclosed. For the sake of saving computer time and storage space, one-half of the channel cross-section was treated. The boundary conditions at the centreline of the channel are:

$$\partial u/\partial z = \partial v/\partial z = \partial\theta/\partial z = 0, \qquad w = \xi = 0 \qquad \text{at } z' = 0.50 \tag{11}$$

The boundary vorticity can be derived from the definition of vorticity and is presented in the numerical method portion. The governing equations subjected to the appropriate boundary conditions will be solved to determine the friction and heat transfer performance which are represented by the friction factor f and the Nusselt number, Nu. The friction factor is defined as:

$$f = \frac{\mu\left(\overline{\frac{\partial U}{\partial N}}\right)_{\text{wall}}}{\frac{1}{2}\rho U_0^2}$$

With a substitution of the characteristic quantities, one obtains

$$fRe = 2\left(\overline{\frac{\partial u}{\partial n}}\right)_{\text{wall}} \tag{12}$$

where n denotes the dimensionless coordinate normal to the wall. The local Nusselt number is defined as:

$$Nu_x = \frac{1}{\overline{\theta}_w - \overline{\theta}} \tag{13}$$

NUMERICAL METHOD

Owing to the complexity of three-dimensional flow, the marching procedure and quasi-non-linear method[12,39] are employed to reduce the computational time taken by a fully implicit scheme. *Figure 2a* shows the staggered mesh employed in the analysis[41–43]. The eccentricity length, H and the length of computation in the x-direction, L_x, are ten and twenty times the duct height, respectively.

The same numerical method is used to determine the axial velocity, axial vorticity and temperature, with different coefficients and different source terms. In the interest of brevity, only the method for the axial velocity is presented here. The upstream data are used in the discretized expression for the axial velocity u^* (before the correction process):

$$a_p u_p^* = a_B u_B + a_E u_E^* + a_W u_W^* + a_N u_N^* + a_S u_S^* + S_u \tag{14}$$

Here,

$$a_E = D_e A(|P_e|) + [-F_e, 0] \qquad a_W = D_w A(|P_w|) + [F_w, 0]$$

$$a_N = D_n A(|P_n|) + [-F_n, 0] \qquad a_S = D_s A(|P_s|) + [F_s, 0]$$

$$a_B = u_B \,\Delta y\, \Delta z$$

$$a_P = a_E + a_W + a_N + a_S + a_B$$

$$S_u = \left\{ -\frac{1}{Re}\left(\overline{\frac{\partial p}{\partial x}}\right) + 2Rov_B - \frac{\eta Gr}{Re^2}\theta_B x \right\} \Delta x\, \Delta y\, \Delta z$$

and the axial pressure gradient is treated as a constant. The coefficients are expressed in the similar forms as in Patankar[41]. The power law scheme is also employed here. The axial velocity thus obtained must satisfy the continuity equation. If not, a new axial pressure gradient is assumed and the computation is repeated for a new axial velocity, until the continuity equation is satisfied. The flow rate through each channel cross-section is calculated using Simpson's rule.

$$u_p = u_p^* + D_p^u\left(\overline{\frac{\partial p}{\partial x}}\right)' \qquad D_p^u = -\frac{1}{Re}\frac{\Delta x\, \Delta y\, \Delta z}{a_p}$$

$$\int u \,dy\, dz = \int u^* \,dy\, dz + \left(\overline{\frac{\partial p}{\partial x}}\right)' \int D^u \,dy\, dz$$

or

$$\left(\overline{\frac{\partial p}{\partial x}}\right)' = \frac{\int u \,dy\, dz - \int u^* \,dy\, dz}{\int D^u \,dy\, dz} \tag{15}$$

The criterion is

$$\left|\frac{\int u^* \, dy \, dz - \int u_0 \, dy \, dz}{\int u_0 \, dy \, dz}\right| \leqslant 10^{-7} \tag{16}$$

The transverse velocity equations (8) and (9) are operated on using the second-order, centred difference method for the differentials in the y and z direction while the three-point backward difference method for the differentials in the axial (x) direction. The criterion of convergence for transverse velocities is:

$$\max\left|\frac{v^n - v^{n-1}}{v^n}\right| \leqslant 5 \times 10^{-5}$$

Here, n is the iteration sequence number.

The numerical scheme used for the boundary vorticity is adopted from Chou[40] to improve the accuracy of computation to the second order (details are listed in Reference 44).

$$\xi_{1,j} = -\xi_{2,j} + \frac{2w_{2,j}}{\Delta y} - \frac{v_{2,j+1} - v_{2,j-1}}{2\zeta \, \Delta z} + O(\Delta y^2, \Delta z^2) \tag{17}$$

The mesh for the boundary vorticity is shown in *Figure 2b*.

The line iteration method with under-relaxation factor is utilized in the computations of u^* and θ in order to improve the convergence speed. The point iteration method is employed in calculating ξ, v and w. The three-point forward (or backward) finite difference scheme is used in the calculations of temperature at walls, gradients for the friction factor and the Nusselt

Table 1 Range of governing parameters used in numerical computations

Parameter	Range
Reynolds No., *Re*	500, 1000, 1500, 2000, 2300
Rossby No., *Ro*	0.0, 0.001, 0.01, 0.1, 0.25, 0.4
Prandtl No., *Pr*	0.70
Heat flux, $q_w a/k$	10.0
Aspect ratio, ζ	0.50, 1.0, 2.0
Length ratio, η	20.0
Eccentricity, h^*/a	10.0

Table 2 Number of meshes used in numerical computations

		Parameter			
Mesh		*Ro* < 0.10	*R*0 = 0.10	*R*0 = 0.25	*Ro* = 0.40
$M \times N$	$\zeta = 0.5$	35 × 35	41 × 41	45 × 45	51 × 51
$(Y \times Z)$	$\zeta = 1.0$	35 × 35	41 × 41	41 × 41	51 × 51
	$\zeta = 2.0$	35 × 68	41 × 81	41 × 81	51 × 101
		Parameter			
Mesh		*Ro* < 0.10	*Ro* = 0.10	0.10 < *Ro* ⩽ 0.25	*Ro* = 0.40
$L(X)$		300	400	500	600

number, to achieve more accurate solutions[42]. The ranges of the parameters for the calculations are listed in *Table 1*. *Table 2* presents the number of meshes used in numerical computations which was determined by numerical convergence experiments. L, M and N are the numbers of nodes in the x-, y- and z-direction, respectively. In *Table 2*, the meshes for the aspect ratio ζ of 0.5 and 1.0 are used on the entire cross-sectional area, while those for $\zeta = 2$ are on one-half of the cross-sectional area to save computing time. The operations, in the order of execution, are:

1. give the initial values of u, v, w, ξ and θ and assign a constant for the axial pressure gradient;
2. solve the axial momentum equation for u^*;
3. calculate new values of u^* by assuming a new axial pressure gradient until the continuity of the main flow rate is satisfied;
4. use the upstream transverse velocities, vorticities and temperature to solve both the axial vorticity transport and boundary vorticity equations for the upgraded vorticity;
6. calculate v, w using the updated u and ξ values;
7. solve the energy equation for temperatures;
8. march from x to $x + \mathrm{d}x$, treat the data solved at x as initial values for $x + \mathrm{d}x$, and return to step 2;
9. repeat steps 2 through 8 until x reaches the desired length.

The CPU required in this scheme was about 7,000 to 30,000 sec on an Apollo-5500 system, depending on the number of meshes used. The discussion of grid independence can be found in Reference 44.

RESULTS AND DISCUSSION

Numerical results were obtained for: (1) the local velocity components, vorticity and temperature, (2) the local friction factor and Nusselt number on the leading, trailing and side walls, and (3) the circumferentially-averaged friction factor and Nusselt number. These results are presented in the forms of: (1) the velocity vector and temperature distribution in the channel cross-section, (2) the axial velocity profiles at the centre of the channel cross-section, (3) the locally-averaged Nusselt number Nu_x on the leading, trailing and side walls, and (4) the circumferentially-averaged $f\,Re$ and Nu. The aspect ratio of the channel cross-section ζ, throughflow Reynolds number, Re, and Rossby number, Ro are varied for laminar flow of air ($Pr = 0.7$) through the channel with iso-flux walls at $q_w = 10k/a$. Some results are presented here for discussing the effects of the governing dimensionless parameters on the friction factor f and the Nusselt number Nu and the roles of the Coriolis force on the transport phenomenon. A square channel, $\zeta = 1.0$, is treated first, which was used as the reference for comparison with a narrow rectangular channel, $\zeta = 0.5$, and a flat rectangular channel with $\zeta = 2.0$. The centripetal buoyancy effect was investigated by varying the characteristic temperature (heat flux) $q_w a/k$ for the case of $Re = 1000$, $Ro = 0.10$ and 0.25, and aspect ratio $\zeta = 1$.

Velocity vector distribution in a channel cross-section

When a square channel begins to rotate at a very low rotational speed, a pair of symmetrical vortices are induced, which circulate from the trailing ($y' = 0$) to leading ($y' = 1.0$) walls along the side walls ($z' = 0$, 1.0) and return from the leading to trailing walls along the channel centreline ($z' = 0.5$), not shown. The vortex cores are located on the lines of $z' = 0.25$ and 0.75. As the rotational speed, Ro, is increased. The vortex cores migrate towards the side walls, accelerating the flows along the side walls and decelerating the flow down the central region. When Ro reaches a certain value, depending upon Re and x, a second pair of vortices appear near the edges of the trailing wall (i.e. corners with the side walls). A further increase in Ro leads to the introduction of a third pair of vortices on the trailing wall and a complex interaction among those vortices ensues.

Figure 3 depicts a series of velocity vector distributions in the channel section under $Re = 2{,}000$ and $Ro = 0.25$ at various locations on the channel axis x. Each vector is composed of the velocity components in the y- and z-direction, respectively. *Figure 3a* at $x = 0.4$ exhibits a pair of the deformed, first (i.e. principal) vortices, the second (near the corners) and third (near the centreline) pairs of vortices on the trailing wall and the fourth pair in the upper (leading wall side) half of the cross-section. As the flow proceeds downstream, the third pair continues to grow, wiping out the second and fourth pairs, see *Figure 3b*, *c* and *d* at $x = 0.6$, 0.8 and 1.0, respectively.

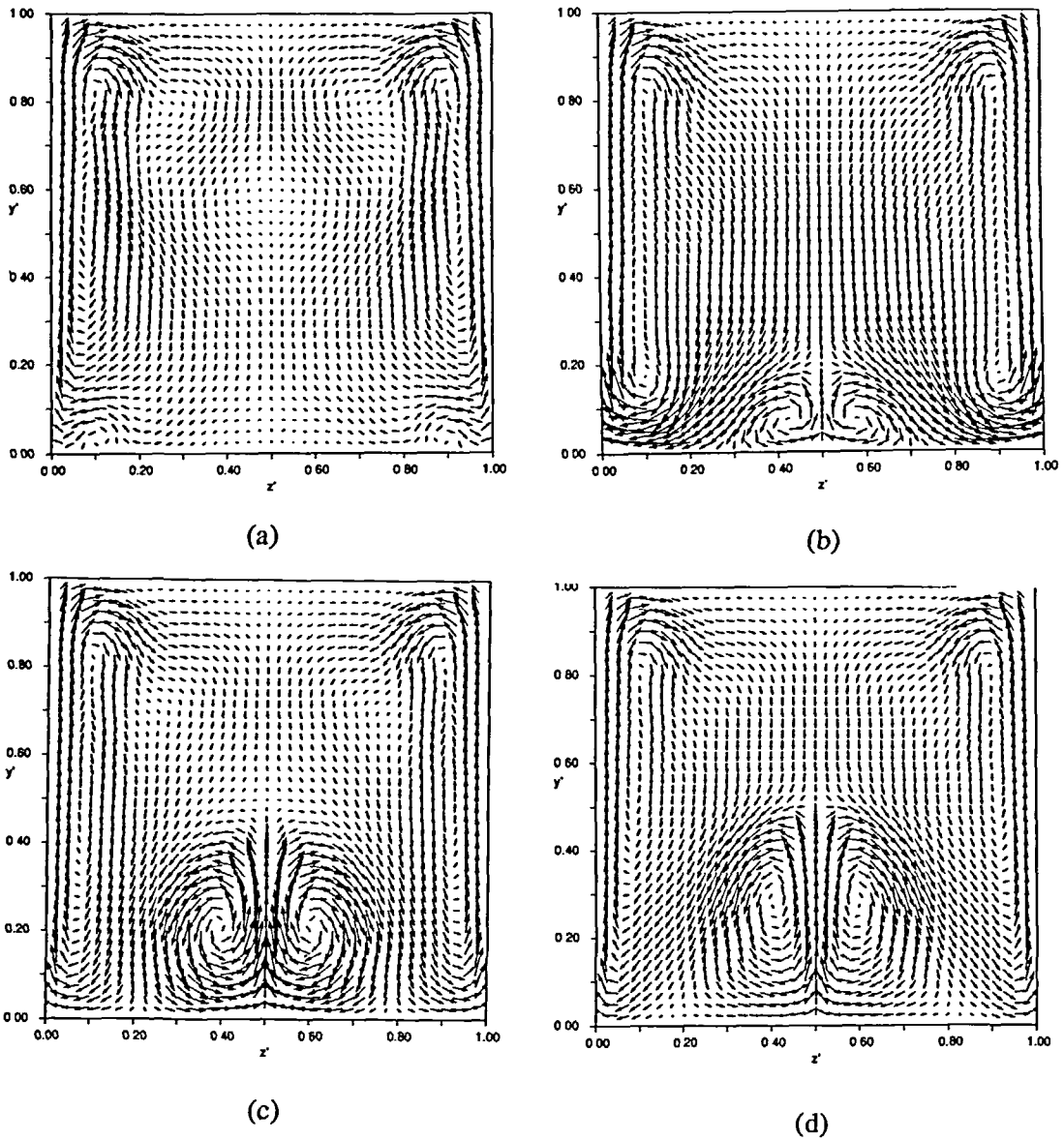

Figure 3 Transverse velocity vector distribution in channel cross section at $Re = 2{,}000$, $Ro = 0.25$, $q_w a/k = 10$, $Pr = 0.7$ and $\zeta = 1.0$, (a) $x = 0.4$, (b) $x = 0.6$, (c) $x = 0.8$ and (d) $x = 1.0$

In comparison with the square channel, the narrow rectangular channel has only the principal pair of vortices as seen in *Figure 4a*. The flat rectangular channel exhibits a completely deformed principal pair of vortices and large second and third pairs on the trailing wall. The vortices completely filled up the trailing half of the cross-section (*Figure 4b*). The effect of rotation on velocity vector can be understood by comparing *Figures 5a* and *b* with *Figure 3d*. There is only one pair of vortices of small magnitude appears at $Ro = 0.010$. In contrast, two small pairs of vortices are induced at very high rotational speed ($Ro = 0.40$) near the trailing wall (*Figure 5b*). A comparison of *Figure 6* and *Figure 3d* reveals the effect of Reynolds number. A higher *Re* results in stronger pairs of the main vortex near the side wall as well as the secondary vortices.

Axial velocity (u) *distribution in a channel cross-section*

Figure 7 depicts the axial velocity (u) distribution in a channel cross-section at different x, with index designating the magnitude of u. It is seen that lower velocities prevail in the leading half of the channel cross-section (i.e. higher y' region) while the trailing half has higher velocities except in the immediate vicinity of the trailing wall. A typical boundary-layer flow phenomena occurs over the side walls. As the flow proceeds downstream, a stratified-flow begins to bulge at the centre ($z' = 0.5$), changing in the shape along the channel. It is of interest to observe changes in the location of the highest axial velocity.

Axial velocity and temperature profiles

A change in the rotational speed, *Ro*, causes variations of both the axial velocity and temperature profiles at $z' = 0.5$ along the flow. Results are presented in *Figures 8* to *11* for

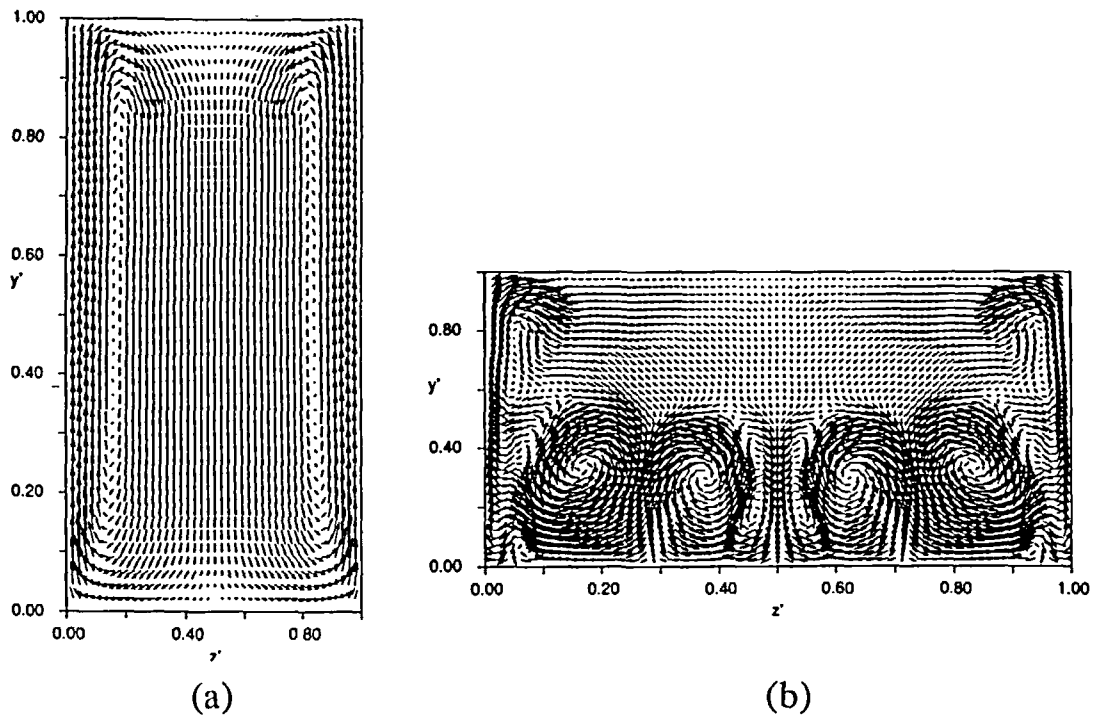

Figure 4 Effects of ζ on velocity vector distribution in channel cross section at $Re = 2{,}000$, $Ro = 0.25$, $q_w a/k = 10$, $Pr = 0.7$ and $x = 1.0$, (a) $\zeta = 0.5$ and (b) $\zeta = 2.0$

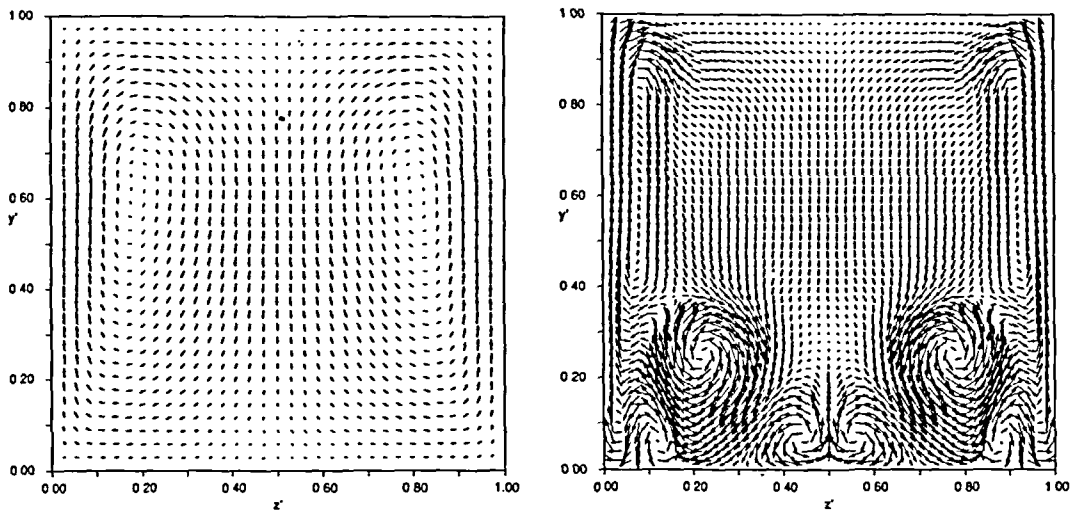

(a) (b)

Figure 5 Effect of Rossby number on velocity distribution in channel cross section at $Re = 2000$, $q_w a/k = 10$, $Pr = 0.7$ and x = 0.7 and x = 1.0, (a) $Ro = 0.010$ and (b) $Ro = 0.40$

$Re = 2{,}000$, at $x = 0.4$, 0.6, 0.8 and 1.0 for different channel cross-sections of $\zeta = 0.5$, 1.0 and 2.0. It should be noted that the uniform velocity and temperature profiles at the entrance $x = 0$ correspond to $u = 1.0$ and $\theta = 0.0$ in the Figures. Here, θ is defined as $(T - T_0)/T_c$. In the absence of rotation, both u and θ are symmetrical with respect to the channel axis, equivalent to the $y' = 0.5$ line. Their profiles change along the channel axis, beginning with a rectangular shape at $x = 0$ and finally taking a parabolic shape at $x = 1.0$. Once rotation is initiated, all the u and θ profiles shift towards the trailing wall, equivalent to the $y' = 0$ line. Take *Figure 8a* at $Ro = 0.01$, for example. At the inlet $x = 0$, u is uniform at 1.0. As the flow reaches $x = 0.4$,

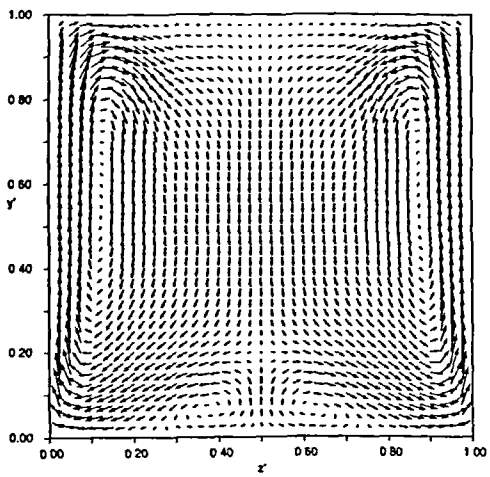

Figure 6 Effect of Reynolds number on velocity distribution in channel cross section at $Re = 1000$, $Ro = 0.25$, $q_w a/k = 10$, $Pr = 0.7$ and $x = 1.0$

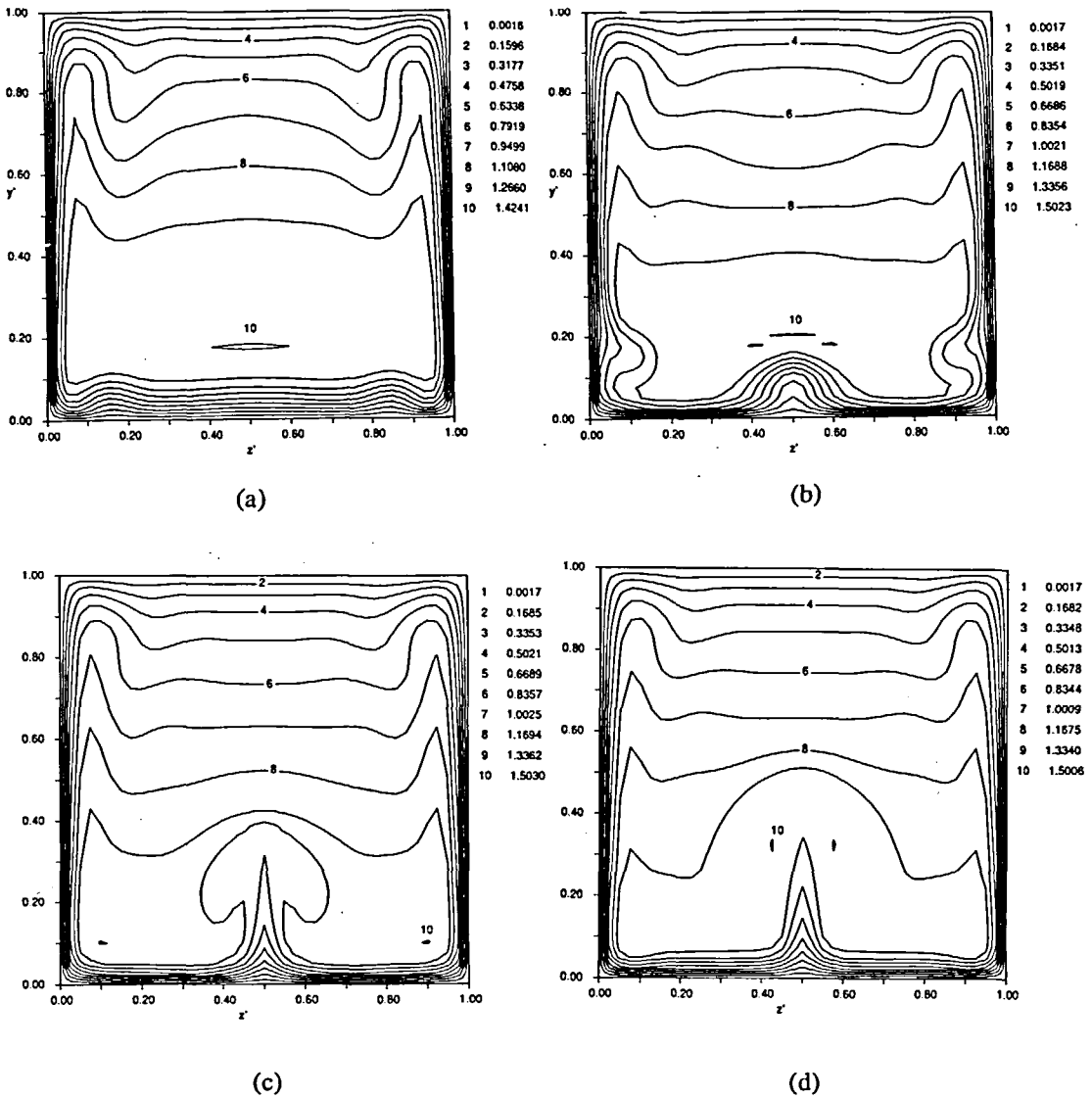

Figure 7 Effects of x on axial velocity distribution in channel cross section at $Re = 2{,}000$, $Ro = 0.25$, $q_w a/k = 10$, $Pr = 0.7$, and $\zeta = 1.0$, (a) $x = 0.4$, (b) $x = 0.6$, (c) $x = 0.8$ and (d) $x = 1.0$

the core is accelerated to u of about 1.35 with its top centre being shifted from $y' = 0.5$ to about 0.35. As the flow proceeds downstream, the core is further accelerated and reduced in size with its centre shifted further towards $y' = 0$. Finally, the profile at the exit $x = 1.0$ takes a skewed parabolic shape with its tip located at $y' \cong 0.25$. It should be noted that the axial velocity gradient on the trailing wall, $(\partial u/\partial y)_{y'=0}$ grows steeper along the flow, while that on the leading wall $(\partial u/\partial y)_{y'=1.0}$ diminishes. This observation has two important implications. One is concerned with the friction performance, higher values of the local friction on the trailing wall and lower values on the leading wall. The other is physical phenomenon that the main flow stream is directed towards the trailing wall, instead of moving parallel to the channel axis. It is referred

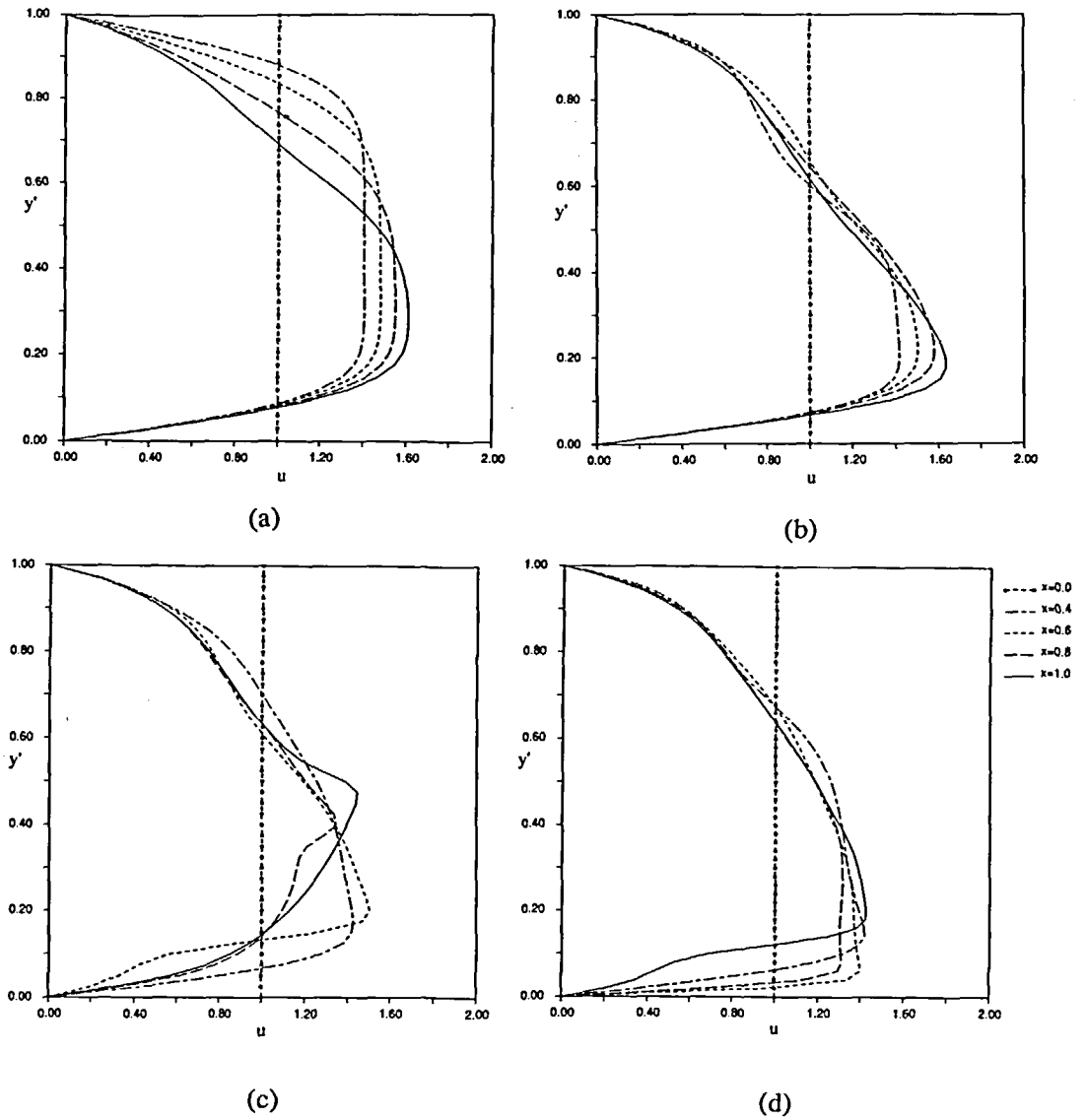

Figure 8 Effects of Ro on variation of axial velocity profile at channel centre ($z' = 0.5$) along channel axis for $Re = 2{,}000$, $q_w a/k = 10$, $Pr = 0.7$, and $\zeta = 1.0$, (a) $Ro = 0.01$, (b) $Ro = 0.1$, (c) $Ro = 0.25$ and (d) $Ro = 0.4$

to as the Ekman flow, which was also observed in a radially outward flow through rotating parallel disks[43]. It results in an enhancement in the convective heat transfer performance. When Ro reaches 0.10, the shifting of the main flow stream towards the trailing wall is further exasperated, as seen in *Figure 8b*. The tip of the deformed parabolic profile is at $y' \cong 0.15$. The velocity profiles on the leading-wall side dent and their tips are at y' of less than 0.2, with the main flow stream strongly washing the trailing wall. In *Figure 8c* for $Ro = 0.25$, a reversal of the profile tip towards the channel axis is observed, from $y' \cong 0.15$ at $x = 0.4$ to $y' \cong 0.47$ at $x = 1.0$. It is accompanied by the denting of the profiles. The deformation of the axial velocity profiles and the reversal of the profile tips are caused by the generation, growth and decay of vortices and by complex interactions among them. The velocity gradients at the trailing wall

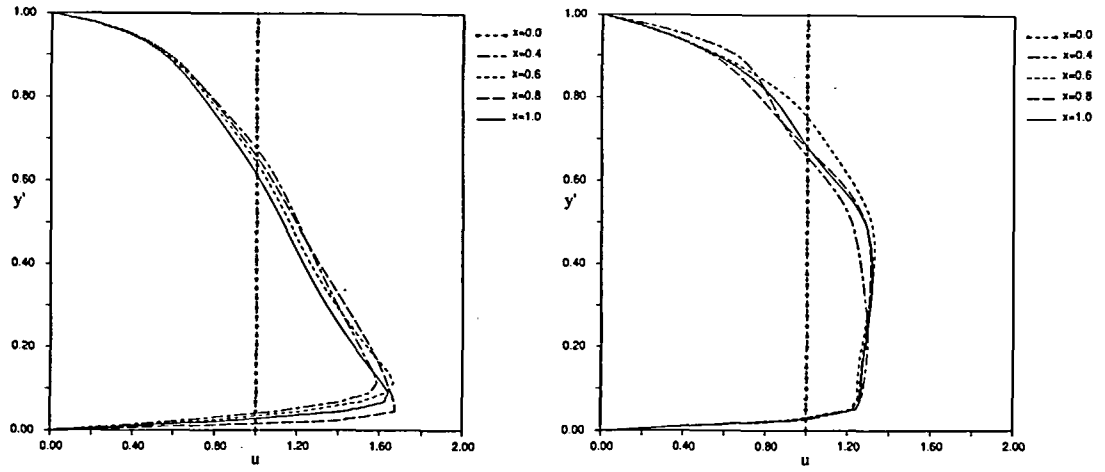

Figure 9 Effects of ζ on variation of axial velocity profiles at channel centre ($z' = 0.5$) along channel axis for $Re = 2{,}000$, $Ro = 0.25$, $q_w a/k = 10$ and $Pr = 0.7$, (a) $\zeta = 0.5$ and (b) $\zeta = 2.0$

fluctuates (increasing followed by decreasing) along the channel axis. The trend of a reversal of a profile tip continues into $Ro = 0.4$, with a strengthening of the tip velocity, as observed in *Figure 8d.*

Figures 9a and *b* depict the development of axial velocities in the narrow and flat rectangular channels, respectively, for a comparison with that in *Figure 8c* for the square channel. The tips of the developing velocity profiles in the narrow rectangular channel get very close to the trailing wall. In contrast, those in the flat rectangular channel are close to the channel axis, with wide tops.

The development of temperature profiles at $z' = 0.5$ is presented in *Figures 10* and *11.* A shift in the axial velocity profile towards the trailing wall results in a similar shift in the temperature profiles, as shown in *Figures 10a* and *b.* This is the mechanism of heat transfer enhancement on the trailing wall and heat transfer degradation on the leading wall due to rotation. In *Figures 10c* and *d* for $Ro = 0.25$ and 0.4, respectively, a reversal in the tip of the developing velocity profiles back towards the channel axis causes a similar phenomenon to occur in the thermal field. Since no boundary condition is specified at the downstream section, the reversal of the trailing wall temperature is due to the secondary vortices developing and varying adjacent to the trailing wall. This is evidenced in the distortions of temperature fields which affect the heat transfer performance on the trailing and leading walls, as illustrated in *Figure 14.*

Figure 11a depicts that the temperature variations in the narrow rectangular channel at $z' = 0.5$ are steep on the trailing wall but gradual on the leading wall than those in the square channel. *Figure 11b* depicts steep and mild temperature variations with wild tops in the flat rectangular channel at $z' = 0.5$.

Friction performance

The friction performance in the entrance region ($0 \leqslant x \leqslant 1$) is expressed in the form of $f\,Re$, where f is the circumferentially-averaged value. Its variation along the channel for $Ro = 0.25$ is illustrated in *Figure 12* as a function of the throughflow Reynolds number, Re. At low values of Re, the variation of $f\,Re$ with x is monotonic, similar to that in the entrance region of a non-rotating channel flow. When Re is increased to 1000, an abrupt decline in $f\,Re$ is immediately

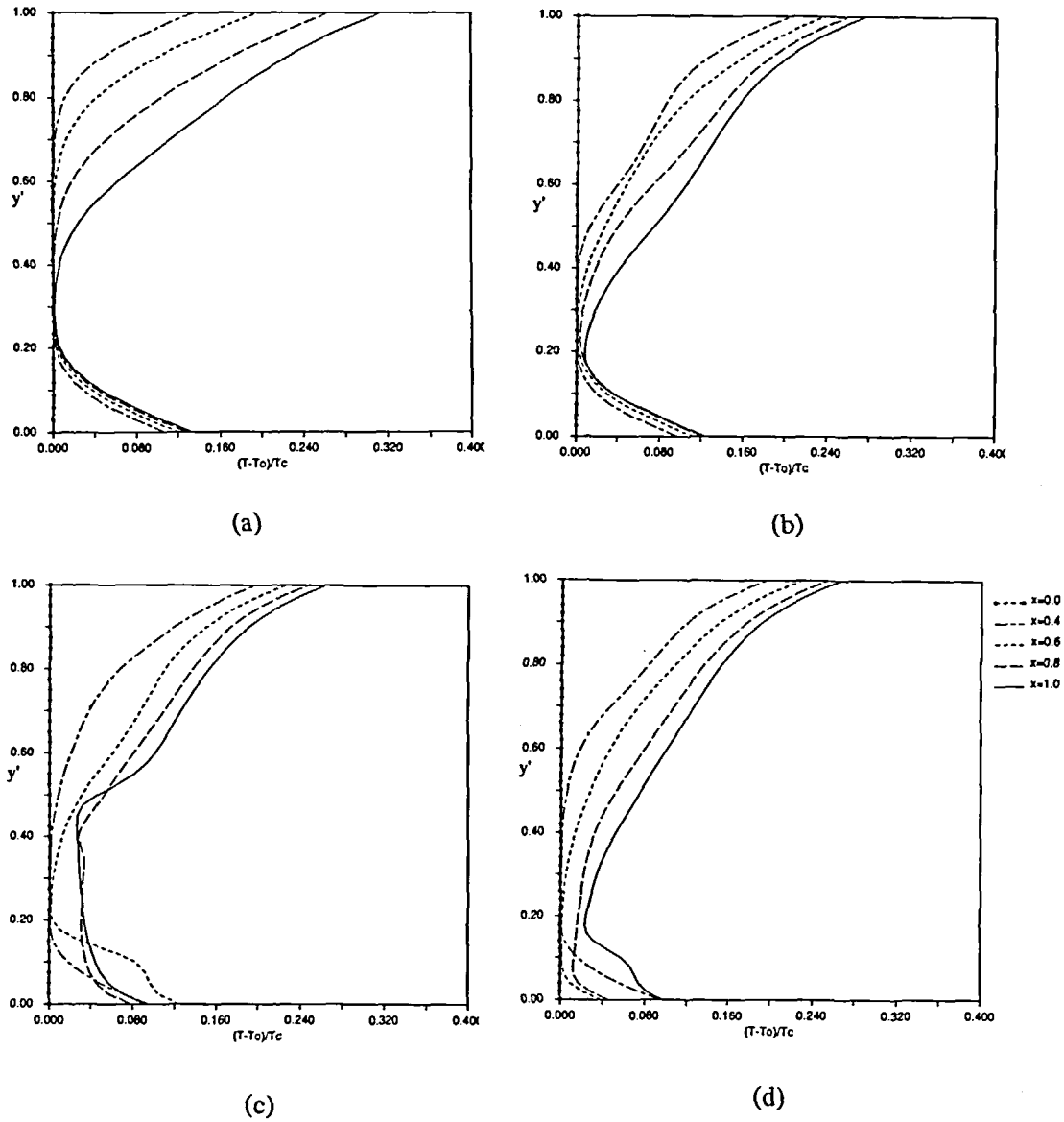

Figure 10 Effects of Ro on variation of temperature profiles at channel centre ($z' = 0.5$) along channel axis for $Re = 2{,}000$, $q_w a/k = 10$, $Pr = 0.7$, and $\zeta = 1.0$, (a) $Ro = 0.01$, (b) $Ro = 0.1$, (c) $Ro = 0.25$ and (d) $Ro = 0.4$

followed by a very minor, short recovery and a second minor recovery at the end. As Re is further increased, the first bump is enhanced with its peak moving downstream, while the second bump near the exit is enhanced more intensely with its peak moving upstream. Now, the third bump appears immediately upstream of the second one. It increases and migrates upstream with an increase in Re. *Figure 12* also depicts the effects of the aspect ratio ζ on $f\,Re$. The $f\,Re$ (equivalently f) values are higher in the narrow rectangular channel and lower in the flat rectangular channel compared with those in the square one. Note the lines for $Re = 2000$ and $\zeta = 0.5$, after the first bump the line goes smoothly until x approaches 0.6 and tends even lower

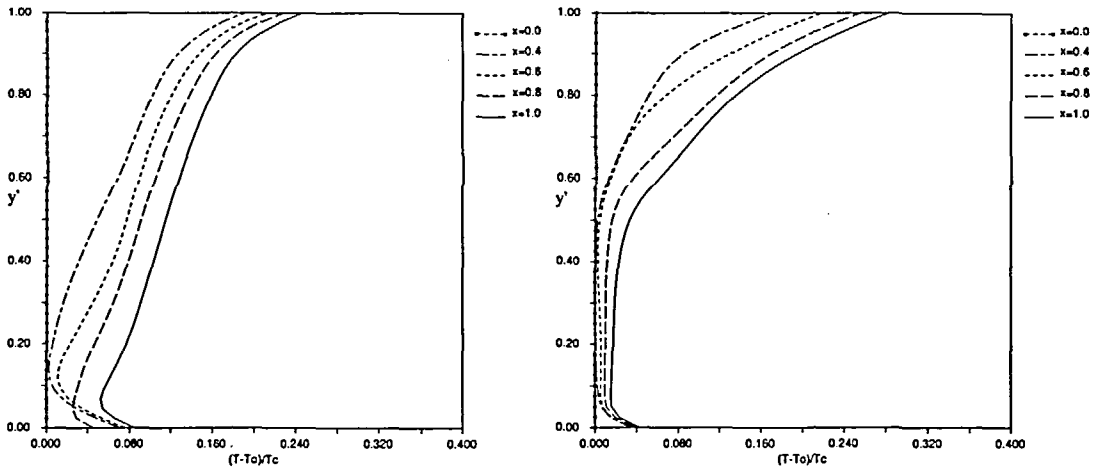

(a) (b)

Figure 11 Effects of ζ on variation of temperature profiles at channel centre ($z' = 0.5$) along channel axis for $Re = 2{,}000$, $Ro = 0.25$, $q_w a/k = 10$, and $Pr = 0.7$, (a) $\zeta = 0.5$ and (b) $\zeta = 2.0$

than the lines for $\zeta = 1.0$ and 2.0 around $x = 0.6$–0.7. This is because no secondary vortices occur before $x = 0.6$ in the narrow channel at $Re = 2000$ and $Ro = 0.25$.

Figure 13 shows the effect of rotation speed on $f\,Re$. It is observed that the $f\,Re$–x relationship is monotonic in the absence of rotation and at a lower rotating speed. In general, the curves become oscillatory with the number and amplitude of oscillations increasing with an increase in Ro.

Heat transfer performance

Both the locally- and circumferentially-averaged heat transfer coefficients, Nu_x and Nu, respectively, are obtained. The former varies depending upon the leading, trailing and side walls.

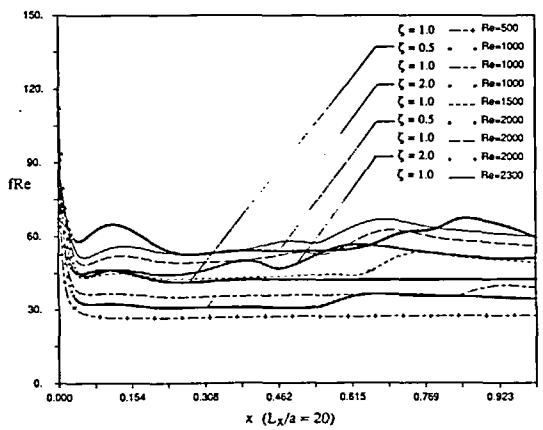

Figure 12 Effects of Re and ζ on variation of circumferentially-averaged friction performance along channel axis for $Ro = 0.25$, $q_w a/k = 10$ and $Pr = 0.7$

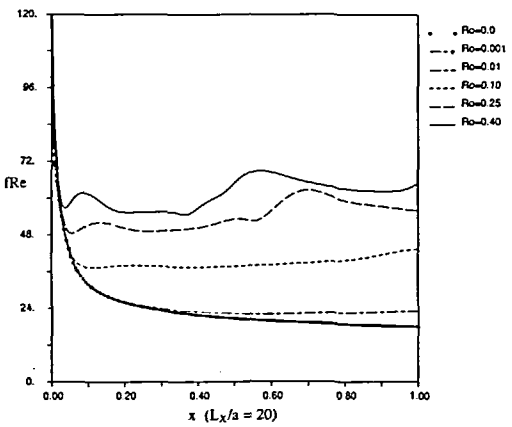

Figure 13 Effects of Ro on variation of circumferentially-averaged friction performance along channel axis for $Re = 2000$, $q_w a/k = 10$, $Pr = 0.7$ and $\zeta = 1.0$

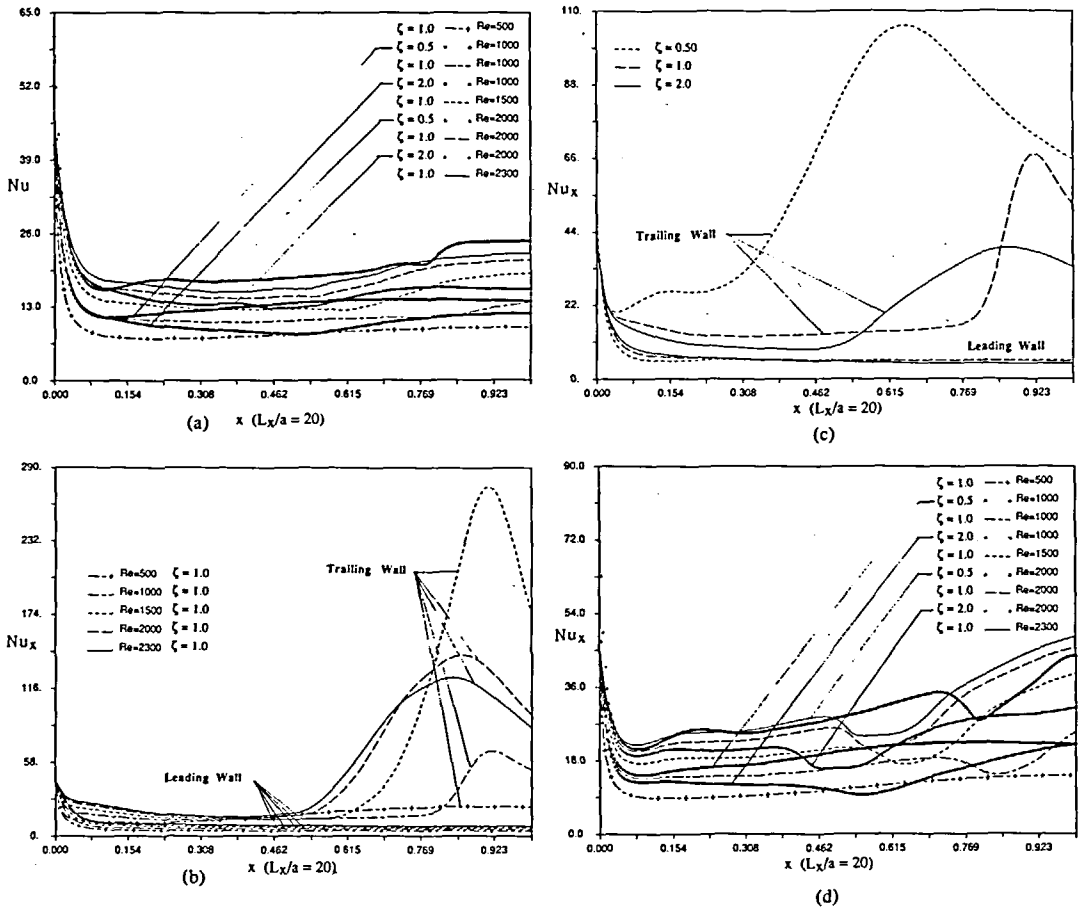

Figure 14 Effects of Re and ζ on variation of heat transfer performance along channel axis at $Ro = 0.25$, $q_w a/k = 10$ and $Pr = 0.7$, (a) circumferentially-averaged Nusselt number, (b) average Nusselt numbers over trailing and leading walls, (c) average Nusselt numbers over trailing and leading walls for $Re = 1000$, and (d) average Nusselt number over side walls

The circumferentially-averaged heat transfer coefficient, Nu, is presented in *Figure 14a*. The Figure indicates a moderate augmentation of Nu with an increase in Re and the square channel is superior to the flat rectangular one, but inferior to the narrow rectangular one. A strong resemblance is observed between the friction performance $f\,Re$ in *Figure 12* and the heat transfer performance Nu in *Figure 14a*, with both f and Nu being circumferentially-averaged values. It is disclosed that (1) Nu increases with a decrease in ζ, and (2) Nu increases as Ro increases but tends to become oscillatory.

Figures 14b and *14c* depict the effects of Reynolds number on Nu_x in the square channel at $Ro = 0.25$. In *Figure 14b*, Nu_x on the leading wall takes a fall near the entrance followed by a gradual decrease to level off. In contrast, Nu_x of the trailing wall varies significantly with Re. At $Re = 500$, a decline in Nu_x is followed by a smooth, moderate recovery towards the end. As Re is increased to 1000 and 1500, Nu_x go under the line for $Re = 500$ first, then a bump appears in the recovery curve near the end. This bump grows very rapidly with its peak moving upstream as Re increases. It is observed that in a square channel the bump peak increases from low Reynolds number and reaches the maximum at $Re = 1500$, then declines as Re is increased

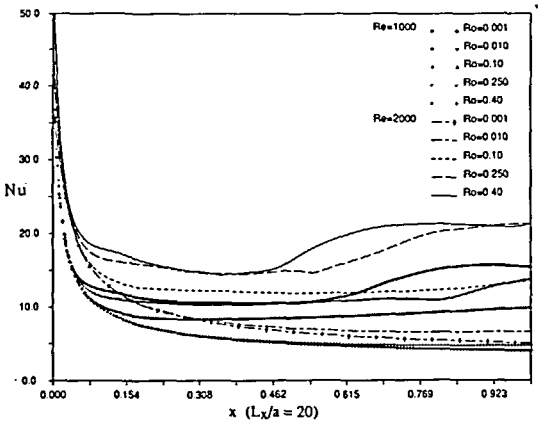

Figure 15 Effects of *Ro* on variation of circumferentially-averaged Nusselt number along channel axis for $Re = 1000$ and 2000, $q_w a/k = 10$, $Pr = 0.7$ and $\zeta = 1.0$

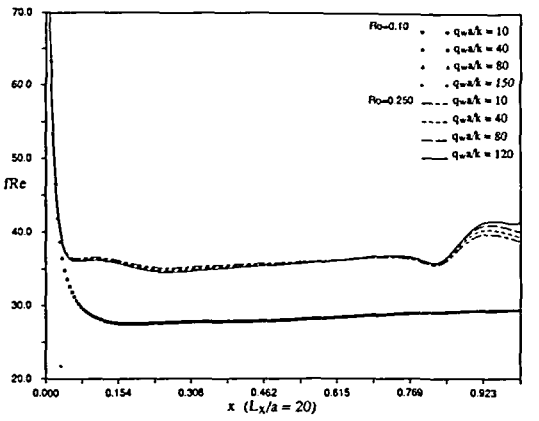

Figure 16 Effects of centripetal buoyancy on variation of circumferentially-averaged friction performance along channel axis for $Re = 1000$, $Ro = 0.10$ and 0.25, $Pr = 0.7$ and $\zeta = 1.0$

further. This behaviour is quite different from that found in the isothermal case[44]. In isothermal case, the bump peak of Nu_x on trailing wall increased with increasing *Re*. *Figure 14c* depicts that at $Re = 1000$, the bump of Nu_x of the flat channel appears earlier than that of the square channel, but also declines earlier. In general, on the leading wall, the square channel is slightly superior to the narrow rectangular one, but slightly inferior to the flat rectangular one. The opposite is true in the case of the trailing wall, where all Nu_x curves exhibit a significant recovery in the downstream half of the channel.

Figure 14d depicts the heat transfer performance of the side walls, which is better than the leading wall but somewhat inferior to the trailing wall. As *Re* increases, the abrupt fall of the Nu_x curves ceases earlier, followed by a gradual recovery before the end. Also found is the abrupt fall for flat channel case appears first, followed by that for square channel and narrow channel, under the same *Re* and *Ro*.

Figure 15 depicts the effects of rotational speed on *Nu*. It is disclosed that at low rotational speeds the Nusselt number displays a smooth growth along the channel axis, but once *Ro* exceeds 0.2, a gradual bump occurs after a small decline. This bump can be attributed to the reversal of the trailing wall temperature (*Figures 10c* and *d*) caused by the emergence of secondary vortices. The lines of $Ro = 0.25$ and 0.40 tend to close to each other after the steep drop from inlet, and jump away downstream, and then close again. Generally, the enhancement of heat transfer from $Ro = 0.25$ to $Ro = 0.40$ is not as impressive as the increase from $Ro = 0.10$ to $Ro = 0.25$.

Centripetal buoyancy effect

The terms with the Grashof number in (2) and (3) represent the effect of the centripetal buoyancy. It is seen in these terms that an increase in either η or *Gr* may result in an increase in the centripetal buoyancy effect. Since the temperature difference in the Grashof number is defined based on the wall heat flux as $Gr = \Omega^2 L_x \beta q_w a^4/(kv^2)$, a linear relationship exists between *Gr* and q_w. *Figures 16* and *17* plot the effects of q_w, or equivalently *Gr*, on $f\,Re$ and the Nusselt number, respectively. The rotational speed, *Ro*, is also varied to investigate its influence on the rotationally-induced natural convection. It is observed in *Figure 16* that under the conditions of $Re = 1000$ and $Ro = 0.10$, the centripetal buoyancy effect is practically unaffected by the heat flux which is increased by 15 times. However, as *Ro* is raised to 0.25, the effect begins to surface:

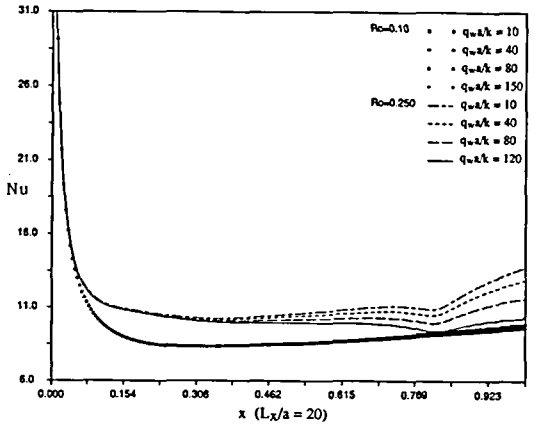

(a)

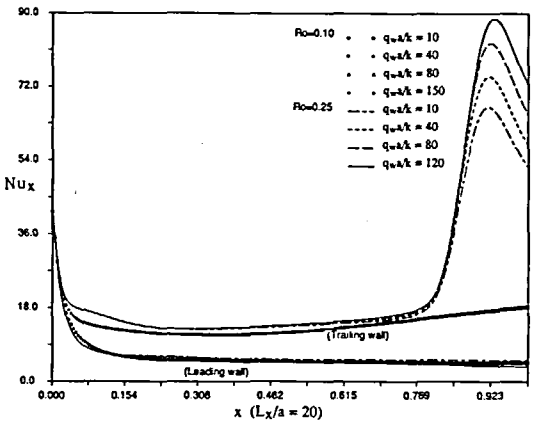

(b)

Figure 17 Effects of centripetal buoyancy on distributtion of heat transfer performance along channel axis at for $Re = 1000$, $Pr = 0.7$ and $\zeta = 1.0$, (a) circumferentially-averaged Nusselt number, (b) average Nusselt numbers over trailing and leading walls, and (c) average Nusselt number over side walls

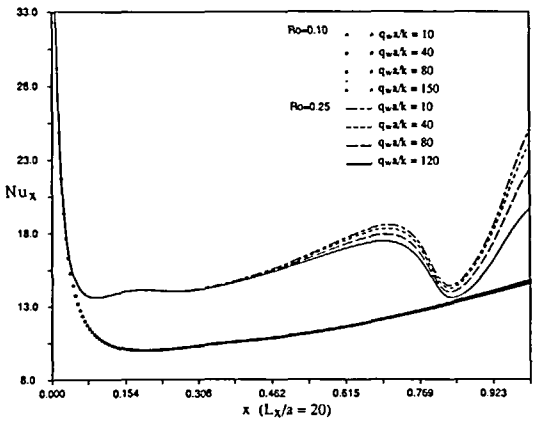

(c)

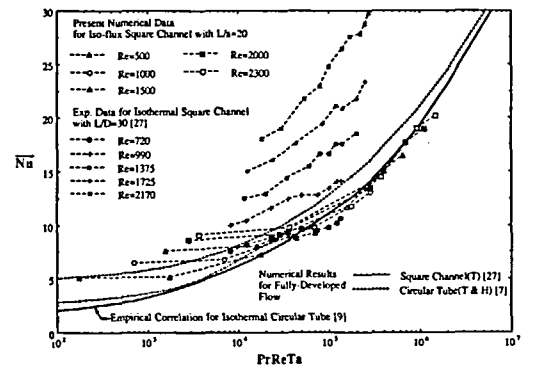

Figure 18 Comparison of present analysis with existing literature

f decreases slightly with an increase q_w near the inlet but increases downstream. *Figures 17a, b* and *c* depict the axial distribution of the circumferentially-averaged Nusselt number, local Nusselt number on the leading and trailing walls, and local Nusselt number on the side walls. It is revealed that an increase- in the wall heat flux results in a reduction of the circumferentially-averaged Nusselt number and local Nusselt numbers on the leading and side walls but an increase of the local Nusselt number on the trailing walls. The reason may be explained as follows: when the centripetal buoyancy is increased due to a raise in the wall heat flux, more flow will be brought into the trailing half. In turn, the continuity of mass requires a reduction of the axial velocity in the leading half, prompting an enhancement of the axial velocity in the trailing half. Consequently, more heat is accumulated in the leading half, thus contributing to an increase in the leading wall temperature. In the mean time, the trailing wall temperature is less affected. The definition of the local Nusselt number in (13) leads to a decrease in the Nusselt number on the leading wall and an enhancement in that on the trailing wall. The present result is in agreement with the experimental observation of Harasgama and Morris[19].

Comparison with literature

The mean values of the circumferentially-averaged heat transfer coefficients (Nu) along the square channels ($0 \leqslant x \leqslant 1$), $\overline{Nu}$, were calculated and displayed in *Figure 18* for a comparison with the existing literature. Four existing results are superimposed in the Figure for comparison: two numerical ones[7,27] and two experimental ones[9,27]. It is seen that the present analysis for $L/a = 20$ underpredicts compared with the experimental data for isothermal square channel ($L/D = 30$). At higher rotational speeds, i.e. $PrReTa \geqslant 3 \times 10^4$, the present model underpredicts compared with the numerical results for developed flow in a circular tube[7] but falls close to the numerical prediction for developed flow in an isothermal square channels[27] and the empirical correlation for isothermal circular tube[9]. It tends to overpredict at lower rotation cases, i.e. $OrReTa$ less than 3×10^4. The overprediction is expected since the present study deals with a developing velocity and temperature case where the entrance effects result in a higher heat transfer performance. The high experimental data of Reference 27 is because their experiments were performed in short channel where the end effect is important.

CONCLUSIONS

The problem of hydrodynamically and thermally developing laminar flow through a rotating channel with uniform heat flux at wall has been formulated. The numerical solution is obtained for air flow using the finite difference technique. The throughflow Reynolds number, Rossby number and aspect ratio of the channel cross-section are varied. The following conclusions are derived from the study.

The Coriolis force causes the generation or decay of vortex pairs on the trailing wall which undergo complex interactions. It results in a higher traverse velocity region in the trailing half, a lower traverse velocity regime in the leading half of the channel cross-section, a shift in the direction of the main flow stream towards the trailing wall (the Ekman flow), a deformation of axial velocity profiles, and a wavering of the profile tips along the flow. Consequently, the thermal field has a higher temperature region in the leading half, a lower temperature region in the trailing half, a deformation of the axial temperature profiles, and a wavering of the profile tips along the channel axis. The effects of rotation include an enhancement of the locally-averaged Nusselt number, Nu_x, on the trailing wall and its fluctuation along the flow, a moderate increase in Nu_x on the side walls, a degradation of Nu_x on the leading wall, an enhancement in both the circumferentially-averaged friction factor f and Nusselt number Nu, and fluctuations of f and Nu along the flow.

In general, both f and Nu are augmented with an increase in the rotational speed Ro and the throughflow rate Re, and a decrease in the aspect ratio of the channel cross-section ζ.

It is also revealed that an increase in the centripetal buoyancy results in a decrease in Nu and Nu_x on the side and leading walls but an increase in Nu_x on the trailing walls.

ACKNOWLEDGEMENT

This study was supported by the Electric Power Research Institute under the EPRI Agreement RP 8006-11.

REFERENCES

1 Ekman, V. W. On the influence of the earth's rotation on ocean currents, *Arkiv. Mat. Astr. Fys.*, **2**, 1–52 (1905)
2 Tritton, D. J. *Physical Fluid Dynamics*, Von Nostrand/Reinhold, London (1977)
3 Yang, Wen-Jei and Zhang, N. Steady thermal and hydrodynamic boundary layer flows with rotation, *4th Int. Symp. Transport Phenomena, Sydney* (July 1991)

4 Barua, S. N. Secondary flow in a rotating straight pipe, *Proc. R. Soc.* (*A*), **227**, 133–139 (1954)
5 Trefethen, L. Laminar flow in radial rotating ducts. *Report R55GL350/55GL350-A*, General Electric Company (1957)
6 Benton, G. S. and Boyer, D. Flow through a rapidly rotating conduit of arbitrary cross-section, *J. Fluid Mech.*, **26**, 69–79 (1966)
7 Mori, Y. and Nakayama, W. Convective heat transfer in rotating radial circular pipe (1st Report, Laminar Region), *Int. J. Heat Mass Transfer*, **11**, 1027–1040 (1968)
8 Ito, H. and Nanbu, K. Flow in rotating straight pipes of circular cross section, *ASME J. Basic Eng.*, **93**, 383–394 (1971)
9 Mori, Y., Fukuda, T. and Nakayama, W. Convective heat transfer in rotating circular pipe (2nd Report), *Int. J. Heat Mass Transfer*, **14**, 1807–1824 (1971)
10 Johnston, J. P., Halleen, R. M. and Lezius, D. K. Effects of spanwise rotation on the structure of two-dimensional fully developed turbulent channel flow, *J. Fluid Mech.*, **56**, 533–557 (1972)
11 Skiadaressis, D. and Spalding, D. B. Heat transfer in a pipe rotating around a perpendicular axis, *ASME Paper No. 77-WA/HT-39* (1977)
12 Patankar, S. V. and Spalding, D. B. A calculation for heat, mass and momentum transfer in three-dimensional parabolic flows, *Int. J. Heat Mass Transfer*, **15**, 1787–1806 (1972)
13 Majumdar, A. K., Pratap, V. S. and Spalding, D. B. Numerical computation of flow in rotating ducts, *ASME J. Fluid Eng.*, **99**, 148–153 (1977)
14 Vidyanidhi, V., Suryanarayana, V. V. S. and Chenchu Raju, V. C. An analysis of steady fully developed heat transfer in a rotating straight pipe, *ASME J. Heat Transfer*, 148–150 (1977)
15 Metzger, D. E. and Stan, R. L. Entry region heat transfer in rotating radial tubes, *AIAA 15th Aerosp. Sci. Meet.*, pp. 77–189 (1977)
16 Howard, J. H. G., Patankar, V. S. and Bordynuik, R. M. Flow prediction in rotating ducts using Coriolis-modified turbulence models, *ASME J. Fluid Eng.*, **102**, 456–461 (1980)
17 Morris, W. D. *Heat Transfer and Fluid Flow in Rotating Coolant Channels*, John Wiley, New York (1981)
18 Morris, W. D. and Ayhan, T. An experimental study of turbulent heat transfer in a tube which rotates about an orthogonal axis, *Proc. XIV ICHMT Symp. Heat Mass Transfer Rotat. Machin., Dubrovnik* (1982)
19 Harasgama, S. P. and Morris, W. D. The influence of rotation on the heat transfer characteristics of circular, triangular, and square-section coolant passages of gas turbine rotor blade, *ASME J. Turbomachin.*, **110**, 44–50 (1988)
20 Speziale, C. G. Numerical study of viscous flow in rotating rectangular ducts, *J. Fluid Mech.*, **122**, 251–271 (1982)
21 Speziale, C. G. and Thangam, S. Numerical study of secondary flows and roll-cell instability in rotating channel flow, *J. Fluid Mech.*, **130**, 377–395 (1983)
22 Siegal, R. Analysis of buoyancy effect on fully developed laminar heat transfer in a rotating tube, *ASME J. Heat Transfer*, **107**, 338–344 (1985)
23 Mansour, K. Laminar flow through a slowly rotating straight pipe, *J. Fluid Mech.*, **150**, 1–21 (1985)
24 Iacovides, H. and Launder, B. E. Turbulent momentum and heat transport in square-sectioned ducts rotating in orthogonal mode, *Num. Heat Transfer*, **12**, 475–491 (1987)
25 Iacovides, H. and Launder, B. E. Parametric and numerical study of fully-developed flow and heat transfer in rotating rectangular ducts, *ASME Paper No. 90-GT-24* (1990)
26 Guidez, J. Study of the convective heat transfer in a rotating coolant channel, *ASME J. Turbomachin.*, **111**, 43–50 (1989)
27 Hwang, G. J. and Jen, T. C. Convective heat transfer in rotating isothermal ducts, *Int. J. Heat Mass Transfer*, **33**, 1817–1827 (1990)
28 Shah, R. K. and London, A. L. *Laminar Flow Forced Convection in Ducts*, Academic Press, New York (1978)
29 Durst, F. and Raszillier, H. Flow in a rotating straight pipe, with a view on Coriolis mass flow meters, *ASME J. Fluid Eng.*, **112**, 149–154 (1990)
30 Raszillier, H., Guiasu, I. and Durst, F. Symbolic computation of flow in a rotating pipe, *Int. J. Num. Meth. Fluids*, **11**, 267–285 (1990)
31 Hajek, T. J. and Higgins, A. W. Coolant passage heat transfer with rotation, *NASA Contract NAS3-23691*, United Technologies Corporation (1984)
32 Kays, W. M. and Crawford, M. E. *Convective Heat and Mass Transfer*, McGraw-Hill, New York (1980)
33 Wagner, J. H., Johnson, B. V. and Hajek, T. J. Heat transfer in rotating passages with smooth walls and radial outward flow, *ASME Paper No. 89-GT-272* (1989)
34 Wagner, J. H., Johnson, B. V. and Kopper, F. C. Heat transfer in rotating serpentine passages with smooth walls, *ASME Paper No. 90-GT-331* (1990)
35 Han, J. C. and Park, J. S. Developing heat transfer in rectangular channels with rib turbulators, *Int. J. Heat Mass Transfer*, **31**, 183–195 (1988)
36 Chandra, P. R., Han, J. C. and Lau, S. C. Effect of rib angle on local heat/mass transfer distribution in a two-pass rib-roughened channel, *ASME J. Turbomachin.*, **110**, 233–241 (1988)
37 Han, J. C. and Zhang, P. Effect of rib-angle orientation on local mass transfer distribution in a three-pass rib-roughened channel, *ASME J. Turbomachin.*, **113**, 123–130 (1991)
38 Taslim, M. E., Rahman, A. and Spring, S. D. An experimental investigation of heat transfer coefficients in a spanwise rotating channel with two opposite rib-roughened walls, *ASME J. Turbomachin.*, **113**, 75–82 (1991)
39 Ramakrishna, K., Rubin, S. G. and Khosla, P. K. Laminar natural convection along vertical square ducts, *Num. Heat Transfer*, **5**, 59–79 (1982)

40 Chou, F. C. Combined free and forced laminar convection in horizontal rectangular channels, *PhD Thesis*, National Tsing Hua University (1986)
41 Patankar, S. V. *Numerical Heat Transfer and Fluid Flow*, Hemisphere, New York (1982)
42 Anderson, D. A., Tannehill, J. C. and Pletcher, R. H. *Computational Fluid Mechanics and Heat Transfer*, Hemisphere, New York (1984)
43 Sim, Y. S. and Yang, Wen-Jei, Numerical study on heat transfer in laminar flow through co-rotating parallel disks, *Int. J. Heat Mass Transfer*, **27**, 1963–1970 (1984)
44 Fann, S. and Yang, Wen-Jei, Hydrodynamically-thermally developing laminar flow through rotating channels having isothermal walls, *Num. Heat Transfer*, in press